High-pressure CaF_2 revisited: A new high-temperature phase and the role of phonons in the search for superionic conductivity

Joseph R. Nelson,[1,*] Richard J. Needs,[1] and Chris J. Pickard[2,3]

[1]*Theory of Condensed Matter Group, Cavendish Laboratory, J. J. Thomson Avenue, Cambridge CB3 0HE, United Kingdom*

[2]*Department of Materials Science and Metallurgy, University of Cambridge, 27 Charles Babbage Road, Cambridge CB3 0FS, United Kingdom*

[3]*Advanced Institute for Materials Research, Tohoku University, 2-1-1 Katahira, Aoba, Sendai 980-8577, Japan*

(Received 13 July 2018; published 11 December 2018)

We recently proposed a high-pressure and high-temperature $P\bar{6}2m$-symmetry polymorph for CaF_2 on the basis of *ab initio* random structure searching and density-functional theory calculations [J. R. Nelson *et al.*, Phys. Rev. B **95**, 054118 (2017)]. We revisit this polymorph using both *ab initio* and classical molecular dynamics simulations. The structure undergoes a phase transition to a superionic phase in which calcium ions lie on a bcc-symmetry lattice (space group $Im\bar{3}m$), a phase not previously discussed for the group-II difluorides. We demonstrate that modeling this phase transition is surprisingly difficult and requires very large simulation cells (at least 864 atoms) in order to observe correct qualitative and quantitative behavior. The prediction of superionic behavior in $P\bar{6}2m$ CaF_2 was originally made through the observation of a lattice instability at the harmonic level in DFT calculations. Using superionic α-CaF_2, CeO_2, β-PbF_2, and Li_2O as examples, we examine the potential of using phonons as a means to search for superionic materials and propose that this offers an affordable way to do so.

DOI: 10.1103/PhysRevB.98.224105

I. INTRODUCTION

Calcium difluoride (CaF_2) has several technological applications, and as a result its electronic structure and properties have been widely studied [1–9]. Under ambient conditions, CaF_2 adopts the cubic fluorite structure (α-CaF_2) with space group $Fm\bar{3}m$. This polymorph of CaF_2 has a number of interesting optical properties, such as intrinsic birefringence [1] and a wide direct band gap at Γ of 12.1 eV [2,3]. The optical gap in α-CaF_2 is calculated to increase with pressure [4,5]. α-CaF_2 and doped variations thereof show good transmittance over a wide range of wavelengths [6], making it an ideal material for optical systems. At high temperatures, α-CaF_2 undergoes a superionic phase transition at $T_c = 1430$ K at ambient pressure, forming β-CaF_2, with F^- ions as the diffusing species [10]. α-CaF_2 is not alone in this regard; superionic phase transitions are ubiquitous in materials with the fluorite structure, such as PbF_2, $SrCl_2$, BaF_2, CeO_2, and Li_2O [11–15].

At high pressures, α-CaF_2 undergoes a phase transition to the denser, orthorhombic cotunnite phase (γ-CaF_2, space group $Pnma$) at around 9 GPa [8] and a further transition to a hexagonal $P6_3/mmc$-symmetry phase at 72 GPa [9]. Experimental data on high-T CaF_2 is scarcer. Currently available data suggest a high-T modification of γ-CaF_2 [16,17] (see also Ref. [18]); however, these data have not yet structurally characterized this phase. Theoretical work has proposed that γ-CaF_2 melts directly at high temperature [19], becomes superionic at high temperature (in the same structure) [20], or undergoes a phase transition to another solid phase which then becomes superionic [17]. Our recent study proposed a $P\bar{6}2m$-symmetry CaF_2 structure as a high-T modification of γ-CaF_2 [5] (Fig. 1). This conclusion was reached through structure prediction calculations [21–23], treating thermodynamics within the quasiharmonic approximation. $P\bar{6}2m$-CaF_2 has the Fe_2P structure and is a known high-T polymorph of $BaCl_2$ and BaI_2 [24,25]; this structure has also been observed in other AB_2 compounds at high pressure such as TiO_2 [26] and ZrO_2 [27]. Whether $P\bar{6}2m$ CaF_2 is a feasible candidate polymorph for high-pressure and -temperature CaF_2 has recently been debated [28–30].

It was also proposed in Ref. [5] that an unstable phonon mode could drive a superionic phase transition in $P\bar{6}2m$ CaF_2 (Fig. 1). This idea, that certain lattice instabilities could trigger a superionic phase transition, was discussed by Boyer for α-CaF_2 and the α-β transition [10] and has been used to infer superionic behavior in a number of materials [14,31].

In this paper, we revisit the proposed $P\bar{6}2m$ CaF_2 structure and explore its high-T behavior through *ab initio* molecular dynamics (AIMD) simulations. We discuss our methods first in Sec. II, before moving on to our results in Sec. III. In Sec. IV, we discuss our results, and we also examine links between phonon frequencies and superionic conductivity. Finally, we report our conclusions in Sec. V.

II. METHODS

AIMD simulations in this paper use the CP2K code [32] and density-functional theory (DFT) with the Perdew-Burke-Ernzerhof (PBE) exchange-correlation functional [33].

*jn336@cam.ac.uk

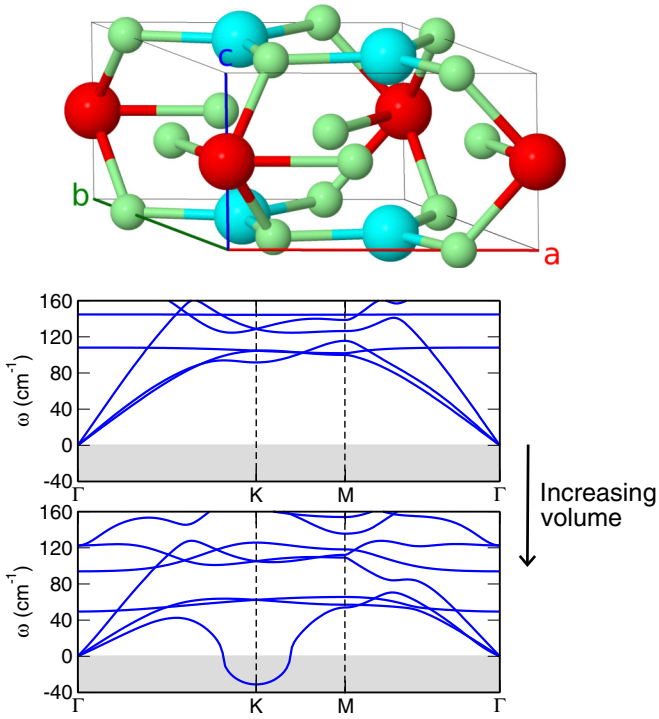

FIG. 1. Top: The $P\bar{6}2m$ CaF_2 structure. Calcium atoms on the 1*b* Wyckoff site are in red, and those on the 2*c* site are in blue. Fluorine atoms are shown in green. Bottom: Phonon dispersion relations in $P\bar{6}2m$ CaF_2 showing the softening of an acoustic mode at *K* at increasing volume (see Ref. [5]).

Goedecker-Teter-Hutter pseudopotentials are used for Ca and F, which treat ten and seven electrons as valence, respectively [34–36]. These are used in conjunction with double-zeta valence polarized (DZVP) "molecularly-optimised (MOLOPT)" Gaussian basis sets [37]. The Γ point is used for Brillouin-zone integration in all AIMD simulations. Simulation cells containing 864 atoms are used in all cases; the reason for this choice of cell size is discussed further in Sec. III A. When compared with larger triple-zeta valence polarized (TZV2P) basis sets, the DZVP basis sets we use deliver energy differences accurate to 4 meV/CaF_2, and the relative average absolute difference in forces and pressures is less than 5% for the two basis sets.

AIMD simulations in the canonical (*NVT*) ensemble use Nosé-Hoover thermostats with a time constant of 100 fs. In these simulations, all lattice parameters are fixed. AIMD simulations in the constant-stress *NPT* ensemble use the same thermostat time constant and a barostat time constant of 2000 fs and allow variation of all lattice parameters $(a, b, c, \alpha, \beta, \gamma)$. Pressure is applied hydrostatically to the simulation cell. A time step of 1 fs is used throughout.

Classical molecular dynamics simulations use the LAMMPS code [38] alongside the same thermostat and barostat time constants given above. Pair potentials used in these simulations are of the Buckingham type and are taken from Ref. [39] for CaF_2 and Ref. [40] for Li_2O.

Phonon frequency calculations use the CASTEP plane-wave code and density-functional perturbation theory [41,42], in conjunction with norm-conserving pseudopotentials generated by the CASTEP code's inbuilt NCP17 pseudopotential library. Phonon frequency calculations using pair potentials are performed with the GULP code [43].

III. RESULTS

A stability field for $P\bar{6}2m$ CaF_2 was proposed at temperatures above 1500–2000 K and at pressures larger than about 10 GPa on the basis of calculations using the quasiharmonic approximation [5]. This section examines the behavior of $P\bar{6}2m$ CaF_2 at 20 GPa and in the temperature range 2500–3000 K.

A. Preliminaries

The thermodynamic conditions 2500 K and 20 GPa lie within the stability field suggested for $P\bar{6}2m$ CaF_2 but not in the region where this structure is predicted to develop a phonon instability according to Ref. [5].

Prior to commencing our AIMD calculations, we use classical molecular dynamics to investigate the simulation cell size needed to obtain converged results, as suggested in Ref. [44]. Here and in what follows, we use an orthorhombic setting (with $Z = 6$) of the hexagonal unit cell of $P\bar{6}2m$ CaF_2 (which has $Z = 3$; see Fig. 1). Convergence is judged by examining both the qualitative and quantitative behaviors of the mean-squared displacement (MSD) of Ca and F ions in $P\bar{6}2m$ CaF_2 as a function of the number of atoms N in the simulation cell. The MSD of a particular set of ions is calculated using

$$\mathrm{MSD}(t) = \frac{1}{M}\sum_i |\mathbf{r}_i(t) - \mathbf{r}_i(0) - [\mathbf{R}_{\mathrm{CM}}(t) - \mathbf{R}_{\mathrm{CM}}(0)]|^2, \tag{1}$$

where $\mathbf{r}_i(t)$ is the position of ion i in the set at time t, $\mathbf{R}_{\mathrm{CM}}(t)$ is the center of mass of the set of ions at time t, and the sum over i runs over all ions in the set, of which there are M in total. Time-windowed averaging is not performed.

Figure 2 shows the MSD of Ca and F ions in $P\bar{6}2m$ CaF_2 at 2500 K and 20 GPa as a function of cell size N. Supercells are constructed to be very roughly cubic for a given N. Uncertainties in the MSD, as indicated by the light blue and orange shaded regions in Fig. 2, are obtained by averaging over 100 trajectories with different initial velocities ($N = 216$, 432, 540, and 864) or 20 trajectories ($N = 15\,552$). The results shown in Fig. 2 were obtained in the *NVT* ensemble; cell sizes for these simulations were obtained by first evolving a cell with $N = 15\,552$ in the *NPT* ensemble and then averaging the corresponding lattice parameters over time.

The results depicted in Fig. 2 show that the convergence of the MSD curves with respect to simulation cell size is slow, and surprisingly large simulation cells are required to see correct qualitative behavior. At small cell sizes ($N = 216$), we observe significant Ca diffusion; we have also observed such behavior in AIMD simulations at this cell size [30]. There is a significant qualitative change in the MSD curves in going from $N = 432$ to $N = 540$: for cells containing fewer than 432 atoms, Ca ions exhibit a greater diffusivity than F ions (as inferred from the slope of the MSD curves), whereas cells with more than 540 atoms show the opposite behavior.

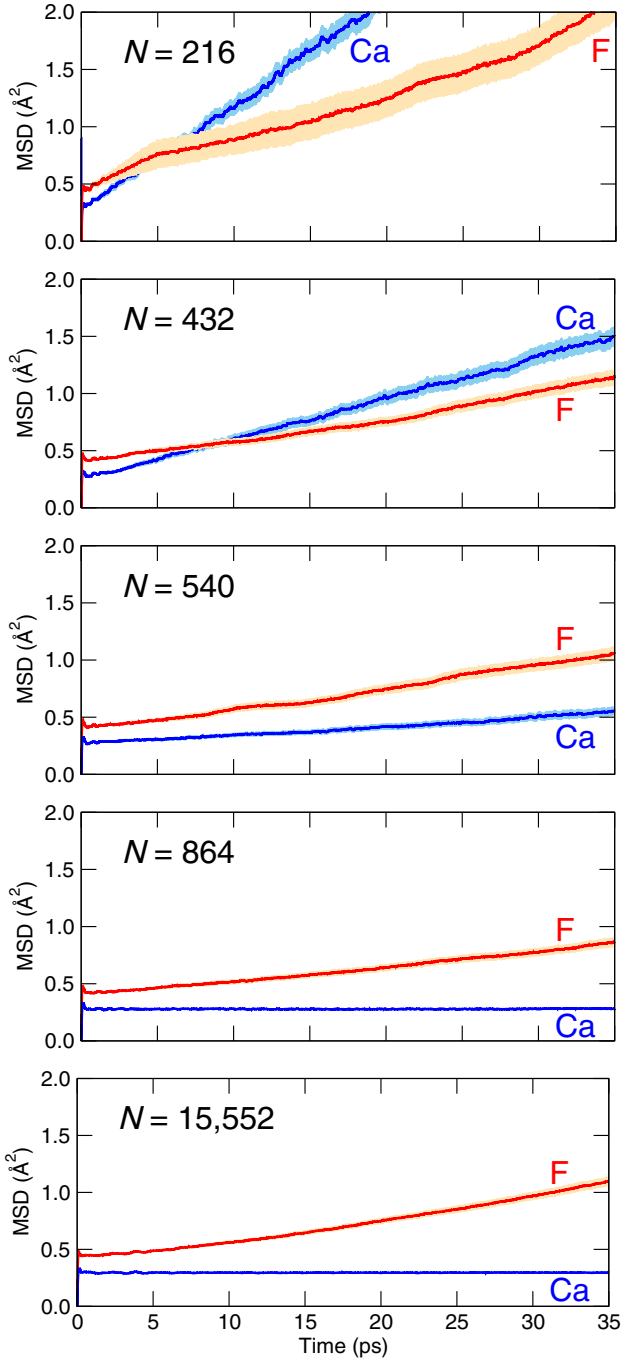

FIG. 2. Behavior of the mean-square displacement of Ca and F ions in the $P\bar{6}2m$ structure as a function of simulation cell size N at $T = 2500$ K and $P = 20$ GPa, from classical MD simulations. Light blue and orange shaded regions indicate the uncertainty in the MSD for Ca and F, respectively, obtained by averaging over multiple trajectories. Note that the uncertainties are small on the scale of the plots for $N = 864$ and $N = 15\,552$.

Referring to Fig. 2, we find that the MSD curves are not qualitatively converged (as judged against $N = 15\,552$) until there are at least 864 atoms in the simulation cell.

The diffusion behavior of Ca in the c direction is slowest to converge, and the most important factor in obtaining the correct qualitative behavior is the use of a simulation cell

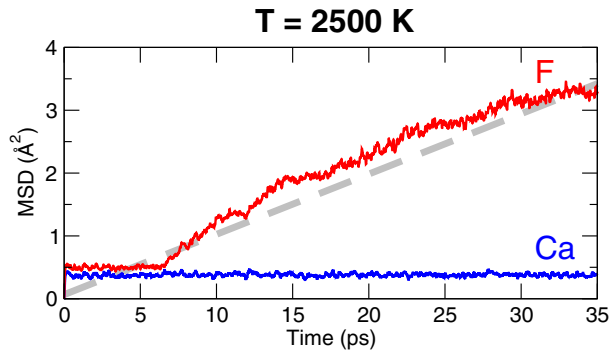

FIG. 3. MSD of F and Ca ions in $P\bar{6}2m$ CaF_2 in an 864-atom AIMD-*NVT* simulation at $T = 2500$ K. The pressure is $P = 19.8 \pm 0.4$ GPa. A best-fit line to the F MSD curve is shown by the thick dashed line.

with a long c axis. Rather than using approximately cubic cells, we can also obtain correct qualitative behavior using a cell which is very elongated in the c direction but uses fewer than 864 atoms, such as for the $2 \times 1 \times 8$ cell given in the Supplemental Material [45]. However, when using such a cell, we find that the fluorine diffusion coefficient is underestimated by 45% compared to the $N = 15\,552$ cell shown in Fig. 2. Better quantitative agreement is obviously obtained when going to larger cells, but we again find quite slow convergence. For our AIMD simulations in the next section, we elect to work with the $N = 864$ cell depicted in Fig. 2. This size of the cell shows correct qualitative behavior in the MSD of Ca and F, although it still underestimates the fluorine diffusion coefficient by 33% when compared against $N = 15\,552$. The 864-atom cell is a $3 \times 2 \times 8$ supercell of the aforementioned orthorhombic $P\bar{6}2m$ unit cell. This also means that it is commensurate with the Brillouin zone K point [46], where a phonon instability was previously reported at sufficiently large volumes [5] (see also Fig. 1). Further MSD curves for other sizes of simulation cell can be found in the Supplemental Material [45].

B. AIMD results

$T = 2500$ K. Figure 3 gives the results of an 864-atom AIMD simulation on $P\bar{6}2m$ CaF_2 at 2500 K and 20 GPa, carried out in the *NVT* ensemble. As was the case for our classical MD simulations, the cell size was calculated by first evolving the system in the *NPT* ensemble. The results agree qualitatively with those obtained from classical MD simulations (Fig. 2) at the same cell size ($N = 864$); however, the diffusivity of F ions is about 8 times larger in the AIMD simulation compared to the classical MD simulation. At this temperature and pressure, $P\bar{6}2m$ CaF_2 exhibits appreciable ionic conductivity, with F ions as the diffusing species. The diffusion coefficient for F is 1.6×10^{-6}cm^2 s^{-1} per the slope of the F MSD curve (thick dashed line in Fig. 3). Assuming the applicability of the Nernst-Einstein equation [47], the corresponding ionic conductivity is $\sigma \sim 10^{-2}\ \Omega^{-1}\ \text{cm}^{-1}$. No diffusion of Ca ions is observed at this temperature and pressure. Averaging the positions of Ca ions over the period shown in Fig. 3 and analyzing the symmetry of the resulting

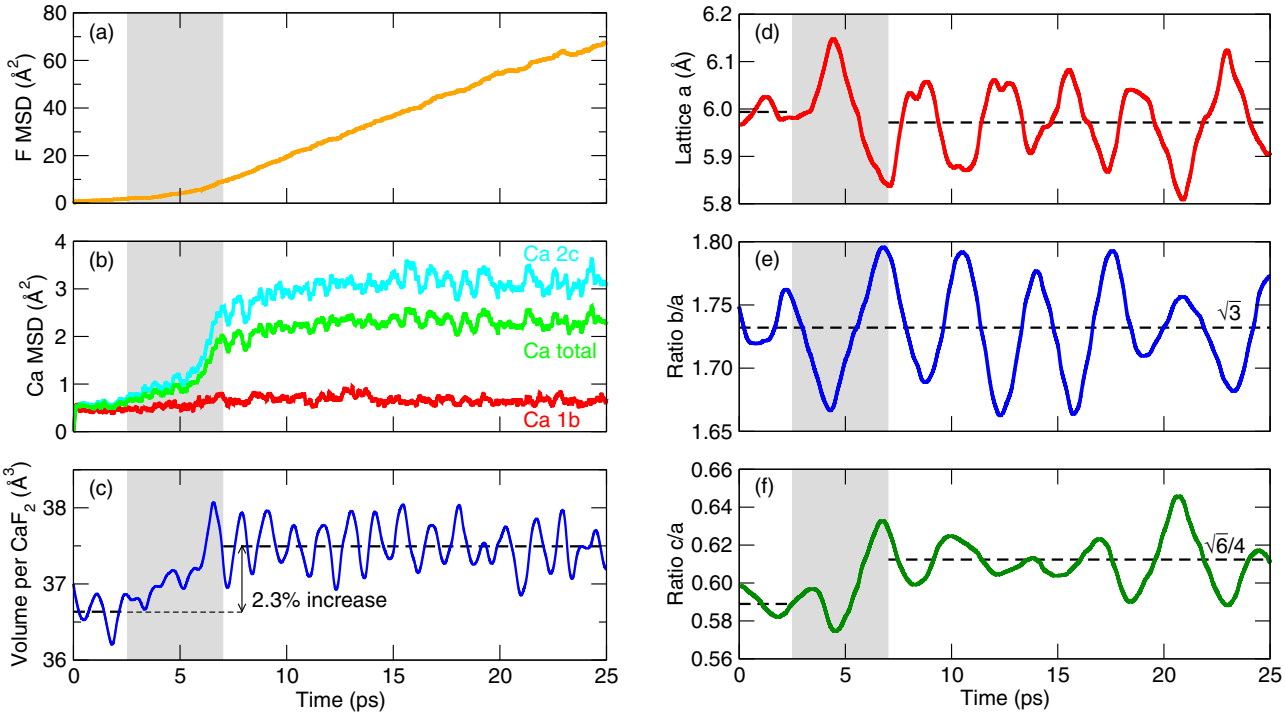

FIG. 4. Results of an 864-atom AIMD-*NPT* simulation at $T = 2650$ K and $P = 20$ GPa. (a) MSD for fluorine. (b) MSD for calcium, split into contributions from calcium ions on the 1*b* and 2*c* Wyckoff sites. (c) Evolution of the system volume. (d) Lattice parameter a for the hexagonal $P\bar{6}2m$ cell. (e) Ratio of the b and a lattice lengths in the orthorhombically set cell. (f) Ratio of the c and a lattice lengths.

structure using the C2X code [48] shows that Ca atoms retain their original positions in the $P\bar{6}2m$ structure. The symmetry of the Ca sublattice alone is $P6/mmm$. We do not observe any structural phase transitions in $P\bar{6}2m$ CaF_2 at 2500 K and 20 GPa, either in the *NVT* simulation shown in Fig. 3 or in the 20-ps-long *NPT* trajectory used to obtain the cell size for the simulation shown in Fig. 3.

T = 2650 K. A set of equilibrated atom positions and velocities is taken from the trajectory shown in Fig. 3 and is evolved in the *NPT* ensemble at 2650 K and 20 GPa. Figures 4(a)–4(f) show the MSD of F and Ca, the volume, and the lattice parameters of the cell as a function of simulation time.

In the *NPT* ensemble, the atomic positions $\mathbf{r}_i(t)$ in Eq. (1) are affected by cell dilations. These show up as slow undulations in the calculated MSDs. To compensate for this, the initial positions $\mathbf{r}_i(0)$ are scaled using the lattice vectors at t via $\mathbf{r}'_i(0) = [\mathbf{a}(t)\ \mathbf{b}(t)\ \mathbf{c}(t)][\mathbf{a}(0)\ \mathbf{b}(0)\ \mathbf{c}(0)]^{-1}[r_{ix}\ r_{iy}\ r_{iz}]^T$, where $\mathbf{a}(t)$, $\mathbf{b}(t)$, and $\mathbf{c}(t)$ are the lattice vectors at time t, and $\mathbf{r}_i(0) = [r_{ix}\ r_{iy}\ r_{iz}]^T$. $\mathbf{r}'_i(0)$ is then used in place of $\mathbf{r}_i(0)$ in Eq. (1) when the MSD is calculated. The initial center-of-mass position $\mathbf{R}_{\mathrm{CM}}(0)$ is similarly scaled. This procedure aids in distinguishing genuine atomic motion from that due to cell dilations.

After a short period (2.5 ps), the cell volume increases and then restabilizes at around the 7-ps mark. The overall volume increase is 2.3% [Fig. 4(c)] and occurs primarily as an expansion in the c direction of the cell (3.4%) accompanied by a small contraction of the a and b axes [Fig. 4(d)]. The hexagonal ratio between the a and b axes, $b/a = \sqrt{3}$, is unchanged [Fig. 4(e)]. The cell remains numerically orthorhombic over the entire trajectory shown in Fig. 4, with $\alpha = 90.2 \pm 0.8°$, $\beta = 90.2 \pm 0.8°$, and $\gamma = 90.0 \pm 1.1°$.

The change in volume is indicative of a phase transition between 2.5 and 7.0 ps, and this time interval is indicated by the gray shaded regions in Fig. 4. After volume expansion, there is a significant increase in F diffusivity [Fig. 4(a)]. Calcium ions on the Wyckoff 1*b* sites in $P\bar{6}2m$ CaF_2 retain their relative positions, while those on the 2*c* sites acquire a permanent displacement away from their initial positions [Fig. 4(b)]. There is a period, after volume expansion, lasting from 7.0 to around 15.0 ps in which the MSD curve for Ca ions on the 2*c* site shows a slow increase before fully stabilizing.

These results are suggestive of a structural rearrangement in the calcium sublattice, which is accompanied by a large increase in fluorine diffusion. Averaging the calcium ion positions and lattice parameters from 15.0 ps onward in the trajectory shown in Fig. 4 and analyzing the symmetry of the resulting structure [48], we find that the calcium ion sublattice is bcc (space group $Im\bar{3}m$).

To summarize, at 2650 K and 20 GPa, we observe a phase transition in $P\bar{6}2m$ CaF_2 in which the calcium sublattice becomes bcc and the fluorine ions display superionic conductivity. The structural changes and sudden increase in ionic conductivity are characteristic of a type-I (abrupt) superionic transition. The bcc superionic state we observe here is reasonably well known in AB_2 compounds: examples include the silver chalcogenides β-Ag_2S and β-Ag_2Se [49,50], and such a state is predicted for high-pressure and high-temperature H_2O [51,52]; however, we are not aware of any previous reports of such a phase in the group-II dihalides. A bcc superionic state

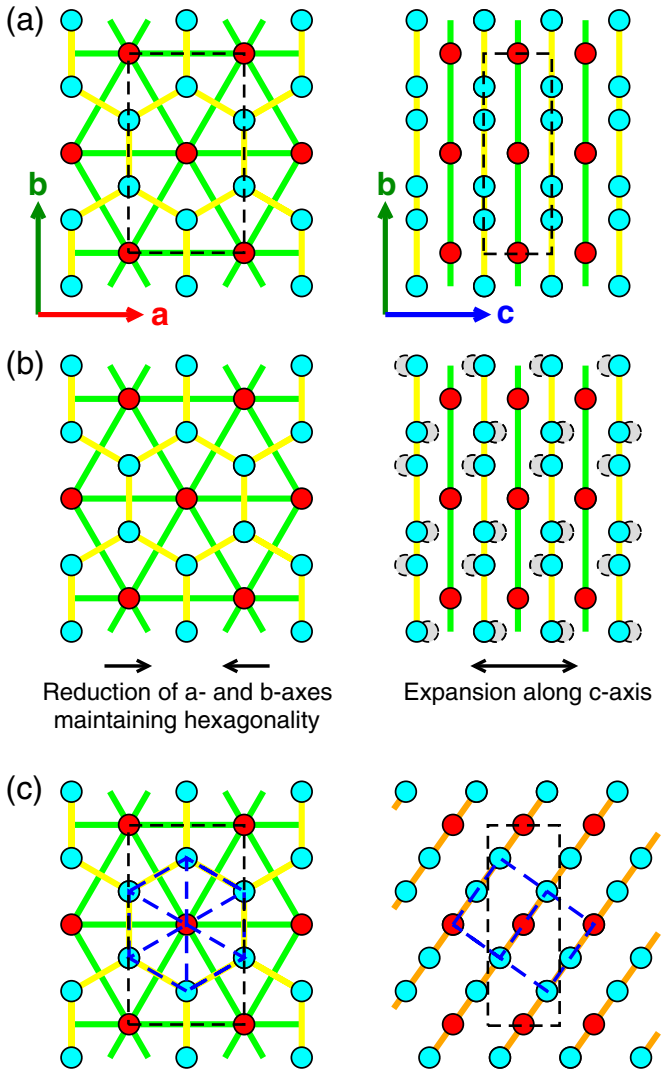

FIG. 5. Changes in the Ca sublattice in $P\bar{6}2m$ CaF_2. Ca ions occupying the 1*b* Wyckoff site are shown in red, and those occupying the 2*c* site are in blue. Yellow and green lines link coplanar Ca ions, in planes perpendicular to the *c* axis. Fluorine ions are not shown. (a) The pristine $P\bar{6}2m$ structure, with black dashed lines showing the orthorhombic cell ($Z = 6$). The hexagonal symmetry means that $b/a = \sqrt{3}$. (b) Increasing temperature results in volume expansion, largely along the *c* axis, with a slight reduction in the *a* and *b* axes. Hexagonality is maintained in the *a* and *b* axes (i.e., $b/a = \sqrt{3}$), and c/a increases to $\sqrt{6}/4$. Ca ions on the 2*c* positions (blue) are displaced away from their sites and onto the sites shown in gray. (c) The resulting Ca sublattice is bcc. The orientation of the conventional bcc unit cell is shown by blue dashed lines.

has been reported in $(PbF_2)_{1-x}(KF)_x$ for $x = 0.333$ [53], with fluorine diffusing, although the cation:anion ratio in this case is 1:1.667 as opposed to 1:2 in CaF_2. Finally, we remark that this transition ($P\bar{6}2m \rightarrow Im\bar{3}m$) can be observed in classical MD simulations, using the same interaction potentials as in Fig. 2.

Figure 5 shows schematically how the calcium sublattice changes during the $P\bar{6}2m \rightarrow Im\bar{3}m$ transition. Calcium ions on Wyckoff 1*b* sites in $P\bar{6}2m$ CaF_2 (red circles in Fig. 5) retain their relative positions, while those on 2*c* sites (blue

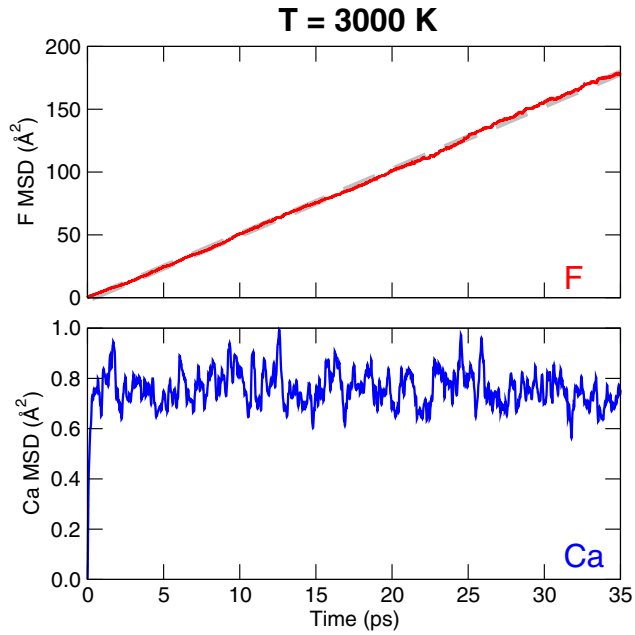

FIG. 6. MSD of F and Ca ions in $P\bar{6}2m$ CaF_2 in an 864-atom AIMD-*NVT* simulation at $T = 3000$ K. The pressure is $P = 19.9 \pm 0.4$ GPa. A best-fit line to the F MSD curve is shown by the thick dashed line.

circles in Fig. 5) are displaced from their initial positions. The net effect of the transition is that these ions end up on new positions, indicated by gray dashed circles in Fig. 5(b). Accompanying this displacement is an expansion along the *c* axis. Figure 5(c) shows, using blue dashed lines, the bcc unit cell. To be consistent with cubic symmetry, we would expect the orthorhombically set $P\bar{6}2m$ cell [black dashed lines in Fig. 5(c)] to have $b/a = \sqrt{3}$ and $c/a = \sqrt{6}/4$, which is what we observe in Figs. 4(e) and 4(f).

$T = 3000$ K. We also carry out an AIMD simulation in the *NVT* ensemble for $Im\bar{3}m$ CaF_2 at 3000 K. The cubic lattice parameter is adjusted so that the pressure is near 20 GPa. Figure 6 gives the MSD of calcium and fluorine from this simulation. The calcium sublattice remains intact, while the diffusion coefficient for F is $8.6 \times 10^{-5} cm^2\,s^{-1}$ (compare 1.6×10^{-6} $cm^2\,s^{-1}$ at 2500 K), corresponding to a Nernst-Einstein conductivity of $\sigma \sim 1\ \Omega^{-1}\,cm^{-1}$ (compare $\sigma \sim 10^{-2}\ \Omega^{-1}\,cm^{-1}$ at 2500 K). Figure 7 shows the fluorine density isosurface at this temperature and pressure, drawn at the density isovalue 0.052 $Å^{-3}$, which corresponds to the mean fluorine density. Heat maps are shown in the (100), (010), and (001) planes, with yellow corresponding to the highest density. As is fairly typical for AB_2-bcc superionic conductors, we see an accumulation of density (yellow regions in Fig. 7) on the tetrahedral and octahedral sites of the immobile sublattice (here calcium).

IV. DISCUSSION

A. AIMD results

The results presented in Sec. III show a high-temperature and high-pressure bcc superionic state in CaF_2 ($Im\bar{3}m$ CaF_2)

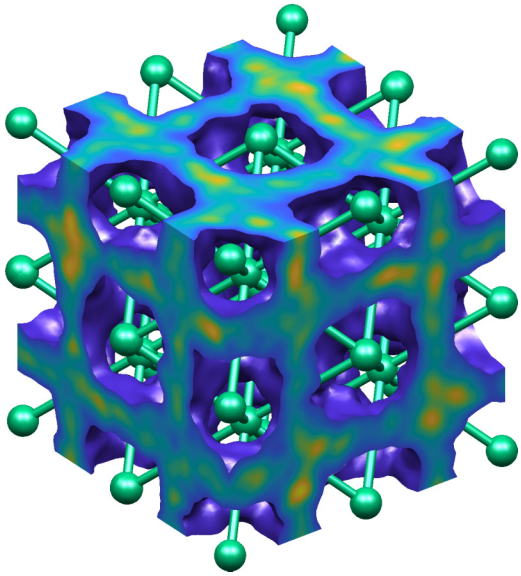

FIG. 7. Fluorine density isosurface for $Im\bar{3}m$ CaF_2 at 3000 K and 20 GPa, drawn at 1 times the mean fluorine density, which is 0.052 $Å^{-3}$. Yellow corresponds to high densities, and blue corresponds to low densities. Calcium ions are represented by pale blue spheres, and a $2 \times 2 \times 2$ supercell of the conventional bcc unit cell is shown. The conventional lattice parameter is 4.24 Å.

formed from a $P\bar{6}2m$-symmetry polymorph at high temperature. This transition was first predicted in Ref. [5] by attributing the onset of a phonon instability at the Brillouin zone K point (Fig. 1) to a superionic phase transition; molecular dynamics simulations were not carried out. The AIMD simulations in the present study indicate that the transition is both structural and superionic, as it involves a structural rearrangement of the calcium sublattice, as well as the onset of high fluorine diffusivity.

We suggested previously that $P\bar{6}2m$ CaF_2 would be stabilized over γ-CaF_2 at high temperatures on the basis of calculations of the γ-$P\bar{6}2m$ Gibbs free-energy difference in the quasiharmonic approximation (QHA) [5]. Combining this with the results of the present work, we anticipate the series of phase transitions γ (cotunnite) $\rightarrow$ $P\bar{6}2m$ $\rightarrow$ superionic $Im\bar{3}m$ with increasing temperature in high-pressure CaF_2. The free-energy differences between γ-CaF_2 and $P\bar{6}2m$ CaF_2 are small, less than 10 meV/CaF_2, even at high temperature [5]. Examples of the cotunnite $\rightarrow$ $P\bar{6}2m$ transition in other materials, such as in ZrO_2 where the transition is pressure induced [27], report similarly small energy differences and suggest that this results in slow kinetics for the transition, giving rise to a reasonably wide coexistence window for both polymorphs (cotunnite and $P\bar{6}2m$). Such a scenario is possible in CaF_2.

The evidence connecting the K-point phonon instability (Fig. 1) to the superionic phase transition seen in Fig. 4 is that the soft-mode eigenvector at K involves displacements of only all F and Ca $2c$ ions and leaves stationary Ca ions on $1b$ sites [5], which is a feature shared by the phase transition (Fig. 5). This is also the case for some of the low-energy (but not soft) phonon modes appearing around 62 cm^{-1} at K in Fig. 1, which show little dispersion along the Γ-K-M-Γ path and leave $2c$ Ca ions stationary along significant portions of this path. In light of this, the superionic phase transition may also involve one of these modes or a combination of the modes discussed here. It is perhaps more conservative to postulate that these phonon modes drive the observed structural phase transition in $P\bar{6}2m$ CaF_2 (to $Im\bar{3}m$ CaF_2) but may not be involved in ion mobility, as some of the phonon modes that will be discussed in Sec. IV B are.

Under PBE exchange correlation, the phonon mode at K is not found to be completely soft at the superionic transition volume: at 20 GPa, the transition occurs at a volume of $1.12V_{\text{static}}$, while full mode softening is seen at $1.17V_{\text{static}}$ [5], where V_{static} is the static-lattice volume of $P\bar{6}2m$ CaF_2 at 20 GPa. This is not necessarily surprising, given that the $P\bar{6}2m$-$Im\bar{3}m$ transition is first order: if there is a soft mode driving this transition, its frequency need not vanish at exactly the transition temperature [54,55].

The AIMD results in Sec. III B differ substantially from AIMD simulations on $P\bar{6}2m$ CaF_2 carried out by previous authors [28,29], where calcium (as opposed to fluorine) diffusion was reported at 20 GPa and 2500 K and a melt state for $P\bar{6}2m$ CaF_2 was reported at 20 GPa and 3000 K. However, it is clear from the results given in Sec. III A that this is because the AIMD simulations in Refs. [28,29] used simulation cells that were not appropriately sized.

B. Phonons and superionicity in fluorite-structured ionic conductors

As raised in Sec. I, Boyer [10] connected a phonon instability at the Brillouin zone X point in fluorite-structured α-CaF_2 to the superionic α-β transition. The soft phonon mode in this case is optical and has B_{1u} mode symmetry. Buckeridge *et al.* [14] have, in addition to the B_{1u} mode, shown a softening of the E_u mode at X in isostructural ceria (CeO_2). We find it instructive to revisit a few more examples of this phenomenon. In Fig. 8, we plot the calculated frequencies of the B_{1u} phonon mode at X for α-CaF_2, CeO_2, and Li_2O and the frequency of the E_u mode for PbF_2 for three common exchange-correlation functionals, the local-density approximation (LDA), PBE, and PBE for solids (PBEsol) [33,56–58], and also give results for a pair potential for Li_2O fitted to bulk properties ("FITEMP" [40]). The choice of mode (B_{1u} or E_u) for each compound corresponds to the mode which first softens at increasing volume, although, as β-PbF_2 demonstrates, both eventually soften at high enough volumes. The reader can also refer to Refs. [5,14,15,59,60] for similar calculations. These four materials are all fluorite structured, and all undergo type-II (continuous) superionic transitions at sufficiently high temperatures. Frequencies are plotted as a function of scaled volume V/V_0, where V_0 is the $T = 0$ K volume for each material as calculated in the quasiharmonic approximation.

Figure 8 also shows, using thick arrows, V/V_0 at the superionic phase transition as derived from experimental data. These values are obtained as follows. For CaF_2, using $T_c =$ 1430 K [10], we deduce V/V_0 from the experimental equation of state (EOS) data of Ref. [61] (left arrow in Fig. 8) and Ref. [62] (right arrow in Fig. 8). For CeO_2, we assume $T_c =$ 2300 K [63] and obtain V/V_0 using the experimental EOS

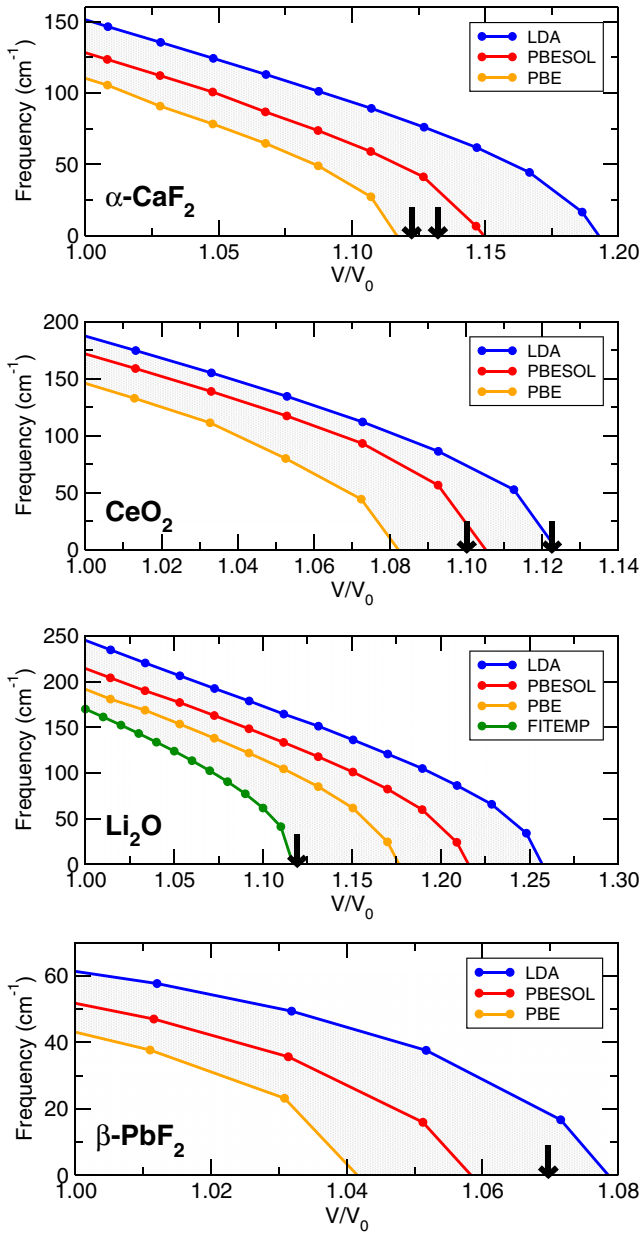

FIG. 8. Softening of the B_{1u} phonon mode in α-CaF_2, CeO_2, and Li_2O and softening of the E_u phonon mode in β-PbF_2 with different exchange-correlation functionals. Frequencies ω are given as a function of relative volume V/V_0, where V_0 is the $T = 0$ K volume. Thick vertical arrows indicate V/V_0 derived from experimental results at the superionic phase transition; see the text for references.

data of Ref. [64] (left arrow) and Ref. [65] (right arrow). For Li_2O, we take $T_c = 1200$ K [15] and use the EOS data of Ref. [66]. Finally, for PbF_2, we take $T_c = 710$ K [11] and use the EOS data of Ref. [67]. V_0 is obtained directly from experimental data where available, otherwise EOS data is extrapolated to 0 K. Data are also extrapolated to T_c if the available data do not extend to high enough temperatures.

The value of V/V_0 corresponding to complete mode softening varies a fair amount between different functionals. From Fig. 8 we observe that, to within the uncertainty introduced by the choice of exchange-correlation functional (LDA, PBE, or PBEsol), there is a softening of either the B_{1u} mode or the E_u mode coincident with the superionic phase transition in α-CaF_2, CeO_2, and β-PbF_2. Complete softening of the B_{1u} mode is found at volumes larger than the transition volume in Li_2O when these three functionals are used; however, the experimental value of V/V_0 at the transition agrees well with V/V_0 where the B_{1u} mode softens when using the aforementioned pair potential for Li_2O. Functional-free techniques for calculating phonon frequencies, such as diffusion Monte Carlo [68], could be used to further clarify this issue.

We close this section by reemphasizing that Fig. 8 and the discussion of phonon frequencies in this section refer to only harmonic phonon frequencies. Recent work on superionic CeO_2 [60] using the temperature-dependent effective potential method [69] has shown that temperature and anharmonic effects impede a complete softening of the B_{1u} phonon mode.

C. Physical role of phonons

A number of physical phenomena are coincident with the onset of a superionic state. Examples include abrupt changes in heat capacities [70], an increase in the number of vacancies, an increase in the number of Frenkel or Schottky defects, an increase in the occupation of interstitial sites [11,53,70–72], a decrease in elastic constants [14,15,66,67,73], and a softening of a particular phonon mode or modes [10,13,14,59,74]. Samara [75] discussed links between materials with a large dielectric constant and superionic behavior, and Annamareddy and Eapen demonstrated the formation of stringlike structures composed of conduction anions [47]. These phenomena are not all independent, and not all of them are observed in every superionic conductor. Of the examples given here, elastic constants, phonon frequencies, and dielectric constants can be accessed through static calculations, as can static defect and/or vacancy energies.

The physical role of phonons—in particular, low-energy or soft-phonon modes—in superionic conduction is described in a number of ways. Diffusing ions tend to move along directions of low curvature on the potential-energy surface, and these directions should, in principle, be detectable through the analysis of phonon modes, by which one can identify low-energy directions for atomic movement. Phonons are effective in moving mobile ions toward saddle points and contribute to diffusive jumps of mobile ions [75,76]. Energy barriers to ionic "hopping" are expected to be smaller for "softer" or more anharmonic lattices [75], and low-lying or soft phonon modes should show strong anharmonicity. As a harmonic phonon mode develops an instability, there is a corresponding increase in amplitude of the softening mode and a concomitant creation of a double-well energy potential [54]. Such a double-well potential can promote defect creation and lead to a higher likelihood of mobile ions occupying interstitial sites [14,60,77] and occurs in a regime in which the potential is too shallow to allow recrystallization into another phase [78]. Previous studies which have either explained or inferred superionic behavior on the basis of phonon modes usually proceeded by analyzing phonon mode eigenvectors and deciding whether there are soft or low-energy modes conducive to disorder or defect creation [5,10,14,79]. Ionic conduction mechanisms proposed based on such analyses

[10] are supported by molecular dynamics calculations [80]. Soft phonon modes have also been used to rationalize self-diffusive behavior, such as that recently discussed in high-PT iron under Earth-core conditions [81]. Experimental neutron-diffraction data suggestive of soft-phonon-mode behavior has been reported in superionic copper selenide [82].

We suggest here that simple descriptors, such as phonon frequencies, offer a viable means by which to screen candidate materials for superionic behavior. The vast majority of structure prediction studies on new materials proceed by first relaxing candidate structures using DFT, then using quasiharmonic lattice dynamics to reassess the stabilities of low-enthalpy crystal structures or to check for dynamic stability [83–85]. This approach is suitable for high-throughput calculations, and numerous predictions made using these techniques have been experimentally verified [86–89]. A wealth of information about harmonic phonons is therefore obtained as a by-product of structure prediction. These data could be combed for low-energy or soft modes whose eigenvectors can be identified with creating disorder, as discussed for $P\bar{6}2m$ CaF_2, α-CaF_2, CeO_2, Li_2O,, and β-PbF_2 in this work. Frequencies of low-energy optical phonons at Γ can also be examined; Wakamura [76] demonstrated a strong correlation between these frequencies and the activation energies required for superionic conduction. Moving away from phonon frequencies, other descriptors such as dielectric constants and ionic sizes [90], elastic constants, and the Lindemann criterion [91] could prove useful in identifying potential superionics.

Directly screening large numbers of candidate materials using AIMD calculations is prohibitively expensive. Efforts are ongoing to substantially reduce the cost of AIMD simulations [92]; however, its computational cost remains very high. Descriptors, such as those discussed here, are suggestive of superionic behavior and could be used as a first step to shortlist a large set of candidate materials or crystal structures for superionicity, after which molecular dynamics simulations can then be carried out. In this work, carrying out AIMD simulations with 864-atom simulation cells on a *single* CaF_2 polymorph ($P\bar{6}2m$ CaF_2) required about an order of magnitude more computing time than that used to search the entire Ca-F structure space in our original work [5]. The latter approach has the added benefit of identifying new stable stoichiometries, such as CaF_3 [5] and BaF_3 and BaF_4 [93] (in the case of superionic BaF_2), which may themselves be candidate superionic materials. It is not necessarily the case that all superionic systems will require large simulation cells, as was the case in this work, but it is difficult to know this *a priori*.

V. CONCLUSIONS

$P\bar{6}2m$ CaF_2, a polymorph suggested to be stable at high temperature and pressure [5], undergoes a type-I superionic phase transition to a bcc superionic state, $Im\bar{3}m$ CaF_2. We have observed this transition in constant-stress NPT simulations working at 2650 K and 20 GPa. The ionic conductivity is calculated to be in the neighborhood of $\sigma \sim 1\ \Omega^{-1}\,\mathrm{cm}^{-1}$ in $Im\bar{3}m$ CaF_2 at 20 GPa and 3000 K.

Modeling the $P\bar{6}2m$ CaF_2 phase at high temperature is difficult. Careful convergence tests need to be carried out to ensure that appropriately sized simulation cells are used. For $P\bar{6}2m$ CaF_2 at 2500 K and 20 GPa, the use of too small a simulation cell leads to the prediction of dominant calcium, rather than fluorine, diffusion, a result that is both qualitatively and quantitatively incorrect. Finite-size effects such as this need to be routinely checked for, and avoided, in molecular dynamics simulations. Where empirical potentials are available, we suggest carrying out such convergence tests using classical MD with a large simulation cell as a benchmark before any AIMD simulations are performed. If appropriate force fields are not available, a series of AIMD tests can still be carried out on small cells to check that diffusion coefficients are converged.

The softening of phonon modes at the Brillouin zone X point is investigated for α-CaF_2, CeO_2, β-PbF_2, and Li_2O as a function of volume. Within the uncertainty due to the treatment of exchange correlation (or choice of pair potential in the case of Li_2O), these compounds exhibit a harmonic phonon instability at fractional volumes V/V_0 corresponding to a superionic phase transition. We have discussed the utility of descriptors, such as soft phonon frequencies, in predicting superionic behavior.

ACKNOWLEDGMENTS

The authors acknowledge useful discussions with Dr. S. Hull, Dr. B. Monserrat, Dr. B. Karasulu, and Prof. A. Walsh. Calculations were carried out using the Archer facility of the United Kingdom's national high-performance computing service, for which access was obtained via the UKCP consortium (Grant No. EP/P022596/1).

[1] J. H. Burnett, Z. H. Levine, and E. L. Shirley, Intrinsic birefringence in calcium fluoride and barium fluoride, Phys. Rev. B **64**, 241102(R) (2001).

[2] G. W. Rubloff, Far-ultraviolet reflectance spectra and the electronic structure of ionic crystals, Phys. Rev. B **5**, 662 (1972).

[3] H. Shi, R. I. Eglitis, and G. Borstel, *Ab initio* calculations of the CaF_2 electronic structure and F centers, Phys. Rev. B **72**, 045109 (2005).

[4] X. Wu, S. Qin, and Z. Wu, First-principles study of structural stabilities, and electronic and optical properties of CaF_2 under high pressure, Phys. Rev. B **73**, 134103 (2006).

[5] J. R. Nelson, R. J. Needs, and C. J. Pickard, High-pressure phases of group-II difluorides: Polymorphism and superionicity, Phys. Rev. B **95**, 054118 (2017).

[6] F. Nakamura, T. Kato, G. Okada, N. Kawaguchi, K. Fukuda, and T. Yanagida, Scintillation and dosimeter properties of CaF_2 transparent ceramic doped with Eu^{2+}, Ceram. Int. **43**, 604 (2017).

[7] S. E. Boulfelfel, D. Zahn, O. Hochrein, Y. Grin, and S. Leoni, Low-dimensional sublattice melting by pressure: Superionic conduction in the phase interfaces of the fluorite-to-cotunnite transition of CaF_2, Phys. Rev. B **74**, 094106 (2006).

[8] P. Kalita, P. Specht, S. Root, N. Sinclair, A. Schuman, M. White, A. L. Cornelius, J. Smith, and S. Sinogeikin, Direct Observations of a Dynamically Driven Phase Transition with *in situ* X-Ray Diffraction in a Simple Ionic Crystal, Phys. Rev. Lett. **119**, 255701 (2017).

[9] S. M. Dorfman, F. Jiang, Z. Mao, A. Kubo, Y. Meng, V. B. Prakapenka, and T. S. Duffy, Phase transitions and equations of state of alkaline earth fluorides CaF_2, SrF_2, and BaF_2 to Mbar pressures, Phys. Rev. B **81**, 174121 (2010).

[10] L. L. Boyer, Nature of Melting and Superionicity in Alkali and Alkaline-Earth Halides, Phys. Rev. Lett. **45**, 1858 (1980).

[11] S. Hull and D. A. Keen, Effect of hydrostatic pressure on the crystal structure and superionic behavior of lead (II) fluoride, Phys. Rev. B **58**, 14837 (1998).

[12] J. Oberschmidt and D. Lazarus, Ionic conductivity, activation volumes, and high-pressure phase transitions in PbF_2 and $SrCl_2$, Phys. Rev. B **21**, 2952 (1980).

[13] K. Schmalzl, Volume and pressure dependence of ground-state and lattice-dynamical properties of BaF_2 from density-functional methods, Phys. Rev. B **75**, 014306 (2007).

[14] J. Buckeridge, D. O. Scanlon, A. Walsh, C. R. A. Catlow, and A. A. Sokol, Dynamical response and instability in ceria under lattice expansion, Phys. Rev. B **87**, 214304 (2013).

[15] M. K. Gupta, P. Goel, R. Mittal, N. Choudhury, and S. L. Chaplot, Phonon instability and mechanism of superionic conduction in Li_2O, Phys. Rev. B **85**, 184304 (2012).

[16] P. W. Mirwald and G. C. Kennedy, Phase relations for SrF_2 to 50 kbars and 1900°C and its compression to 40 kbars at 25°C, J. Phys. Chem. Solids **41**, 1157 (1980).

[17] C. Cazorla and D. Errandonea, Superionicity and Polymorphism in Calcium Fluoride at High Pressure, Phys. Rev. Lett. **113**, 235902 (2014).

[18] P. W. Mirwald and G. C. Kennedy, The phase relations of calcium fluoride (fluorite) to 60 kbars and 1800°C, J. Phys. Chem. Solids **39**, 859 (1978).

[19] Z. Zhao-Yi, C. Xiang-Rong, Z. Jun, and H. Cui-E, Phase transition and melting curves of calcium fluoride via molecular dynamics simulations, Chin. Phys. Lett. **25**, 230 (2008).

[20] C. Cazorla and D. Errandonea, High-pressure, high-temperature phase diagram of calcium fluoride from classical atomistic simulations, J. Phys. Chem. C **117**, 11292 (2013).

[21] C. J. Pickard and R. J. Needs, High-Pressure Phases of Silane, Phys. Rev. Lett. **97**, 045504 (2006).

[22] C. J. Pickard and R. J. Needs, *Ab initio* random structure searching, J. Phys.: Condens. Matter **23**, 053201 (2011).

[23] R. J. Needs and C. J. Pickard, Perspective: Role of structure prediction in materials discovery and design, APL Mater. **4**, 053210 (2016).

[24] A. Haase and G. Brauer, Hydratstufen und Kristallstrukturen von Bariumchlorid, Z. anorg. allg. Chem. **441**, 181 (1978).

[25] H. P. Beck, A structure refinement of the high pressure modification BaI_2-II, J. Solid State Chem. **47**, 328 (1983).

[26] H. Dekura, T. Tsuchiya, Y. Kuwayama, and J. Tsuchiya, Theoretical and Experimental Evidence for a New Post-Cotunnite Phase of Titanium Dioxide with Significant Optical Absorption, Phys. Rev. Lett. **107**, 045701 (2011).

[27] D. Nishio-Hamane, H. Dekura, Y. Seto, and T. Yagi, Theoretical and experimental evidence for the post-cotunnite phase transition in zirconia at high pressure, Phys. Chem. Miner. **42**, 385 (2015).

[28] C. Cazorla, A. K. Sagotra, M. King, and D. Errandonea, High-pressure phase diagram and superionicity of alkaline earth metal difluorides, J. Phys. Chem. C **122**, 1267 (2018).

[29] C. Cazorla and D. Errandonea, Comment on "High-pressure phases of group-II difluorides: Polymorphism and superionicity,"Phys. Rev. B **98**, 186101 (2018).

[30] J. R. Nelson, R. J. Needs, and C. J. Pickard, Reply to "Comment on 'High-pressure phases of group-II difluorides: Polymorphism and superionicity,"'Phys. Rev. B **98**, 186102 (2018).

[31] L. L. Boyer, First-principles theory of phase transformations in ionic solids, Ferroelectrics **35**, 83 (1981).

[32] J. Hutter, M. Iannuzzi, F. Schiffmann, and J. VandeVondele, CP2K: Atomistic simulations of condensed matter systems, WIREs Comput. Mol. Sci. **4**, 15 (2014).

[33] J. P. Perdew, K. Burke, and M. Ernzerhof, Generalized Gradient Approximation Made Simple, Phys. Rev. Lett. **77**, 3865 (1996); **78**, 1396 (1997); **80**, 891 (1998).

[34] S. Goedecker, M. Teter, and J. Hutter, Separable dual-space Gaussian pseudopotentials, Phys. Rev. B **54**, 1703 (1996).

[35] C. Hartwigsen, S. Goedecker, and J. Hutter, Relativistic separable dual-space Gaussian pseudopotentials from H to Rn, Phys. Rev. B **58**, 3641 (1998).

[36] M. Krack, Pseudopotentials for H to Kr optimized for gradient-corrected exchange-correlation functionals, Theor. Chem. Acc. **114**, 145 (2005).

[37] J. VandeVondele and J. Hutter, Gaussian basis sets for accurate calculations on molecular systems, J. Chem. Phys. **127**, 114105 (2007).

[38] S. Plimpton, Fast parallel algorithms for short-range molecular dynamics, J. Comput. Phys. **117**, 1 (1995); LAMMPS, `http://lammps.sandia.gov`.

[39] S. Faraji, S. A. Ghasemi, S. Rostami, R. Rasoulkhani, B. Schaefer, S. Goedecker, and M. Amsler, High accuracy and transferability of a neural network potential through charge equilibration for calcium fluoride, Phys. Rev. B **95**, 104105 (2017).

[40] T. Oda, Y. Oya, S. Tanaka, and W. J. Weber, Validation of potential models for Li_2O in classical molecular dynamics simulation, J. Nucl. Mater. **367–370**, 263 (2007).

[41] S. J. Clark, M. D. Segall, C. J. Pickard, P. J. Hasnip, M. I. J. Probert, K. Refson, and M. C. Payne, First principles methods using CASTEP, Z. Kristallogr. - Cryst. Mater. **220**, 567 (2005).

[42] K. Refson, P. R. Tulip, and S. J. Clark, Variational density-functional perturbation theory for dielectrics and lattice dynamics, Phys. Rev. B **73**, 155114 (2006).

[43] J. D. Gale, GULP: A computer program for the symmetry-adapted simulation of solids, J. Chem. Soc., Faraday Trans. **93**, 629 (1997).

[44] A. D. Mulliner, P. C. Aeberhard, P. D. Battle, W. I. F. David, and K. Refson, Diffusion in Li_2O studied by non-equilibrium molecular dynamics for $873 < T/K < 1603$, Phys. Chem. Chem. Phys. **17**, 21470 (2015).

[45] See Supplemental Material at http://link.aps.org/supplemental/10.1103/PhysRevB.98.224105 for mean-square displacement curves of Ca and F for a variety of simulation cell shapes and sizes.

[46] J. H. Lloyd-Williams and B. Monserrat, Lattice dynamics and electron-phonon coupling calculations using nondiagonal supercells, Phys. Rev. B **92**, 184301 (2015).

[47] A. Annamareddy and J. Eapen, Low dimensional string-like relaxation underpins superionic conduction in fluorites and related structures, Sci. Rep. **7**, 44149 (2017).

[48] M. J. Rutter, C2x: A tool for visualisation and input preparation for Castep and other electronic structure codes, Comput. Phys. Commun. **225**, 174 (2018).

[49] B. H. Grier, S. M. Shapiro, and R. J. Cava, Inelastic neutron scattering measurements of the diffusion in β-Ag_2S, Phys. Rev. B **29**, 3810 (1984).

[50] F. Kirchhoff, J. M. Holender, and M. J. Gillan, Structure, dynamics, and electronic structure of liquid Ag-Se alloys investigated by *ab initio* simulation, Phys. Rev. B **54**, 190 (1996).

[51] H. F. Wilson, M. L. Wong, and B. Militzer, Superionic to Superionic Phase Change in Water: Consequences for the Interiors of Uranus and Neptune, Phys. Rev. Lett. **110**, 151102 (2013).

[52] J.-A. Hernandez and R. Caracas, Superionic-Superionic Phase Transitions in Body-Centered Cubic H_2O Ice, Phys. Rev. Lett. **117**, 135503 (2016).

[53] S. Hull, P. Berastegui, S. G. Eriksson, and N. J. G. Gardner, Crystal structure and superionic conductivity of PbF_2 doped with KF, J. Phys.: Condens. Matter **10**, 8429 (1998).

[54] G. Venkataraman, Soft modes and structural phase transitions, Bull. Mater. Sci. **1**, 129 (1979).

[55] K. Binder, Theory of first-order phase transitions, Rep. Prog. Phys. **50**, 783 (1987).

[56] D. M. Ceperley and B. J. Alder, Ground State of the Electron Gas by a Stochastic Method, Phys. Rev. Lett. **45**, 566 (1980).

[57] J. P. Perdew and A. Zunger, Self-interaction correction to density-functional approximations for many-electron systems, Phys. Rev. B **23**, 5048 (1981).

[58] J. P. Perdew, A. Ruzsinszky, G. I. Csonka, O. A. Vydrov, G. E. Scuseria, L. A. Constantin, X. Zhou, and K. Burke, Restoring the Density-Gradient Expansion for Exchange in Solids and Surfaces, Phys. Rev. Lett. **100**, 136406 (2008); **101**, 239702 (2008); **102**, 039902(E) (2009).

[59] K. Schmalzl, D. Strauch, and H. Schober, Lattice-dynamical and ground-state properties of CaF_2 studied by inelastic neutron scattering and density-functional methods, Phys. Rev. B **68**, 144301 (2003).

[60] J. Klarbring, N. V. Skorodumova, and S. I. Simak, Finite-temperature lattice dynamics and superionic transition in ceria from first principles, Phys. Rev. B **97**, 104309 (2018).

[61] B. Schumann and H. Neumann, Thermal expansion of CaF_2 from 298 to 1173 K, Cryst. Res. Technol. **19**, K13 (1984).

[62] R. J. Angel, The high-pressure, high-temperature equation of state of calcium fluoride, CaF_2, J. Phys.: Condens. Matter **5**, L141 (1993).

[63] M. A. Kovalenko and A. Ya. Kupryazhkin, Melting and superionic transition of Gd-doped ceria nanocrystals: Molecular dynamics study, J. Nucl. Mater. **430**, 12 (2012).

[64] M. Yashima, S. Kobayashi, and T. Yasui, Crystal structure and the structural disorder of ceria from 40 to 1497 °C, Solid State Ionics **177**, 211 (2006).

[65] S. Omar, E. D. Wachsman, J. L. Jones, and J. C. Nino, Crystal structure-ionic conductivity relationships in doped ceria systems, J. Am. Ceram. Soc. **92**, 2674 (2009).

[66] S. Hull, T. W. D. Farley, W. Hayes, and M. T. Hutchings, The elastic properties of lithium oxide and their variation with temperature, J. Nucl. Mater. **160**, 125 (1988).

[67] M. H. Dickens, W. Hayes, M. T. Hutchings and W. G. Kleppmann, Neutron scattering studies of acoustic phonon modes in PbF_2 up to high temperatures, J. Phys. C **12**, 17 (1979).

[68] Y. Y. F. Liu, B. Andrews, and G. J. Conduit, Vibrational modes and atomic relaxation in Diffusion Monte Carlo, DPG Spring Meeting of the Condensed Matter Section, 11-16 March 2018, Berlin, Abstract no. MM 57.6 (unpublished).

[69] O. Hellman, P. Steneteg, I. A. Abrikosov, and S. I. Simak, Temperature dependent effective potential method for accurate free energy calculations of solids, Phys. Rev. B **87**, 104111 (2013).

[70] D. A. Keen, S. Hull, A. C. Barnes, P. Berastegui, W. A. Crichton, P. A. Madden, M. G. Tucker, and M. Wilson, Nature of the superionic transition in Ag^+ and Cu^+ halides, Phys. Rev. B **68**, 014117 (2003).

[71] D. A. Keen, S. Hull, W. Hayes, and N. J. G. Gardner, Structural Evidence for a Fast-Ion Transition in the High-Pressure Rock-salt Phase of Silver Iodide, Phys. Rev. Lett. **77**, 4914 (1996).

[72] S. Hull, S. T. Norberg, I. Ahmed, S. G. Eriksson, and C. E. Mohn, High temperature crystal structures and superionic properties of $SrCl_2$, $SrBr_2$, $BaCl_2$ and $BaBr_2$, J. Solid State Chem. **184**, 2925 (2011).

[73] R. K. Singh, C. N. Rao, and S. P. Sanyal, Temperature dependence of elastic constants of some fluorite crystals, Phys. Rev. B **39**, 13493 (1989).

[74] L. L. Boyer, Origin of superionicity in the alkaline earth halides, Solid State Ionics **5**, 581 (1981).

[75] G. A. Samara, High-pressure studies of ionic conductivity in solids, Solid State Phys. **38**, 1 (1984).

[76] K. Wakamura, Roles of phonon amplitude and low-energy optical phonons on superionic conduction, Phys. Rev. B **56**, 11593 (1997).

[77] P. S. Ghosh, A. Arya, G. K. Dey, N. Kuganathan, and R. W. Grimes, A computational study on the superionic behavior of ThO_2, Phys. Chem. Chem. Phys. **18**, 31494 (2016).

[78] L. L. Boyer, Relating double wells to phase transitions from *ab initio* model calculations, Ferroelectrics **111**, 63 (1990).

[79] W. Bührer and P. Brüesch, Phonon dispersion and $\beta \rightarrow \alpha$ transition in silver iodide, Solid State Commun. **16**, 155 (1975).

[80] L. X. Zhou, J. R. Hardy, and H. Z. Cao, Dynamical simulations of superionicity in alkaline-earth halides, Solid State Commun. **98**, 341 (1996).

[81] A. B. Belonoshko, T. Lukinov, J. Fu, J. Zhao, S. Davis, and S. I. Simak, Stabilization of body-centred cubic iron under inner-core conditions, Nat. Geosci. **10**, 312 (2017).

[82] S. A. Danilkin, M. Yethiraj, and G. J. Kearley, Phonon dispersion in superionic copper selenide: Observation of soft phonon modes in superionic phase transition, J. Phys. Soc. Jpn. **79**, 25 (2010).

[83] J. R. Nelson, R. J. Needs, and C. J. Pickard, Calcium peroxide from ambient to high pressures, Phys. Chem. Chem. Phys. **17**, 6889 (2015).

[84] M. Mayo and A. J. Morris, Structure prediction of Li-Sn and Li-Sb intermetallics for lithium-ion batteries anodes, Chem. Mater. **29**, 5787 (2017).

[85] A. Shamp and E. Zurek, Superconducting high-pressure phases composed of hydrogen and iodine, J. Phys. Chem. Lett. **6**, 4067 (2015).

[86] I. Errea, M. Calandra, C. J. Pickard, J. R. Nelson, R. J. Needs, Y. Li, H. Liu, Y. Zhang, Y. Ma, and F. Mauri, High-Pressure Hydrogen Sulfide from First Principles: A Strongly Anharmonic Phonon-Mediated Superconductor, Phys. Rev. Lett. **114**, 157004 (2015).

[87] I. Errea, M. Calandra, C. J. Pickard, J. R. Nelson, R. J. Needs, Y. Li, H. Liu, Y. Zhang, Y. Ma, and F. Mauri, Quantum hydrogen-bond symmetrization in the superconducting hydrogen sulfide system, Nature (London) **532**, 81 (2016).

[88] Y. Li, L. Wang, H. Liu, Y. Zhang, J. Hao, C. J. Pickard, J. R. Nelson, R. J. Needs, W. Li, Y. Huang, I. Errea, M. Calandra, F. Mauri, and Y. Ma, Dissociation products and structures of solid H_2S at strong compression, Phys. Rev. B **93**, 020103(R) (2016).

[89] L. E. Marbella, M. L. Evans, M. F. Groh, J. Nelson, K. J. Griffith, A. J. Morris, and C. P. Grey, Sodiation and desodiation via helical phosphorus intermediates in high-capacity anodes for sodium-ion batteries, J. Am. Chem. Soc. **140**, 7994 (2018).

[90] J. C. Bachman, S. Muy, A. Grimaud, H.-H. Chang, N. Pour, S. F. Lux, O. Paschos, F. Maglia, S. Lupart, P. Lamp, L. Giordano, and Y. Shao-Horn, Inorganic solid-state electrolytes for lithium batteries: Mechanisms and properties governing ion conduction, Chem. Rev. **116**, 140 (2016).

[91] B. Monserrat, M. Martinez-Canales, R. J. Needs, and C. J. Pickard, Helium-Iron Compounds at Terapascal Pressures, Phys. Rev. Lett. **121**, 015301 (2018).

[92] L. Kahle, A. Marcolongo, and N. Marzari, Modeling lithium-ion solid-state electrolytes with a pinball model, Phys. Rev. Mater. **2**, 065405 (2018).

[93] D. Luo, Y. Wang, G. Yang, and Y. Ma, Barium in high oxidation states in pressure-stabilized barium fluorides, J. Phys. Chem. C **122**, 12448 (2018).